Velocity and Concentration Measurements of Supersonic Underexpanded Jets

Carlo Sanapo[1,*], Sara G. Ruiz[1], Charline Fouchier[1], Sebastien Courtiaud[2], Delphine Laboureur[1]

1: Dept. of Environmental and Applied fluid dynamics, von Karman Institute for Fluid Dynamics, Belgium
2: Commissariat a l'Energie Atomique, DAM, France
*Corresponding author: carlo.sanapo@vki.ac.be

Keywords: Supersonic flows, Dispersion, Jet, Large-scale PIV, Light extinction spectroscopy, ABL.

ABSTRACT

The release of high-speed jets (Ma > 1) due to pressurized tank leakage poses a substantial safety hazard as it can give rise to flammable, explosive, or toxic mixtures. Thus, understanding the dispersion of supersonic underexpanded jets within an Atmospheric Boundary Layer (ABL) is essential for ensuring industrial process safety, aerospace applications, or environmental protection. The present work gives an overview of the ongoing phenomenon characterization using non-intrusive optical techniques such as Large-Scale PIV for the velocity measurements. A Mie-Scattering theory-based technique allowed a relative concentration field characterization description. Later through Light Extinction Spectroscopy, an absolute concentration value can be extrapolated from the transmittance spectrum of a light beam passing through a reference zone within the jet.

1. Introduction

High-pressure tanks and piping still play a key role when pressurized substances need to be handled, stored, and later used (e.g., in energy production sites, pharmaceutical, aerospace, or food and beverage.) Routine inspections of pressurized vessels continue to identify a significant number of damaged vessels in workplaces, posing risks of leaks or ruptures OSHA (1999-2023). The potential health and safety hazards of leaking vessels include poisoning, suffocation, fire, explosion, or, even worse, a combination of these. Therefore, ensuring the safe design, installation, operation, and maintenance of pressure vessels or pressurized lines, guided by established standards, is critical for minimizing risks to worker safety and health Zhang & Wang (2022). Although good safety levels have been achieved concerning the design and maintenance of these systems, the incident statistics concerning vessel ruptures show that improvements are still needed OSHA (1999-2023); Zhang & Wang (2022). What is needed is an approach aimed at predicting the most catastrophic event. Implementing a proactive approach to identify and mitigate potential risks before they escalate is crucial, especially when dealing with high-pressurized gas jet dispersion, as it

can pose significant safety hazards if not properly managed. Specifically, when a high-pressurized tank is damaged (e.g., by an orifice-like rupture), a supersonic underexpanded jet is produced: a high-speed, unsteady, not only compressible but also highly turbulent fluid flow which progresses through different stages of spatio-temporal scales (see Fig.1). The characterization and accurate prediction of jet dispersion into the atmosphere, whether within or outside the influence of an Atmospheric Boundary Layer (ABL), are paramount for effectively designing and enhancing safety systems and facility layouts.

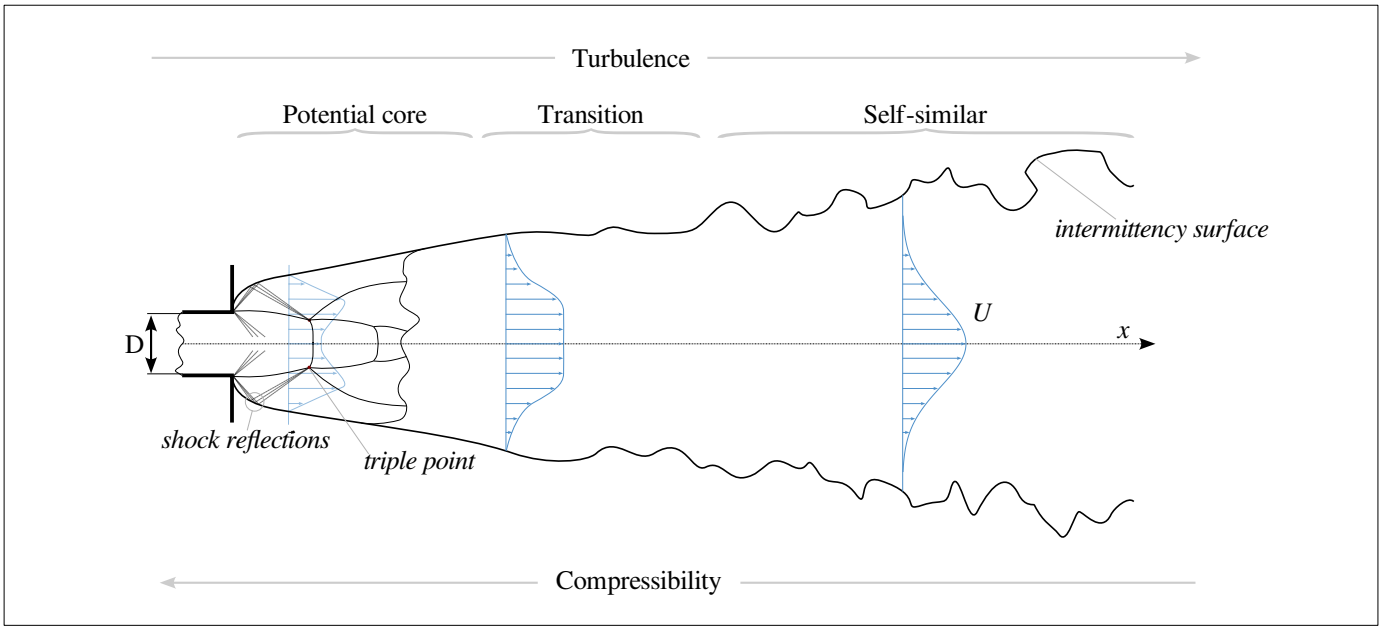

Figure 1. Simplified schematic evolution of a supersonic underexpanded jet.

Dispersion modeling* utilize mathematical formulations to describe how pollutants emitted from a source disperse into the atmosphere. The significant differences between the available models necessitate careful consideration when selecting the appropriate model for each application. Factors such as environmental complexity, model dimensions, computing power, and desired accuracy must be taken into account. Despite limitations, models should be used to provide concentrations within an appropriate degree of error and time period. Furthermore, the absence of validation studies that offer simultaneous concentration and velocity measurements makes validation very challenging Holmes & Morawska (2006); Cleaver & Edwards (1990). Consequently, advanced optical measurement techniques are essential for evaluating jet penetration, mixing, and dispersion Sharmishtha & Utpal (2017).

In addition, most studies are motivated by the fascinating structures of the jet potential core (e.g., Prandtl-Meyer expansion, Mach disk, diamond pattern, triple points, Prandtl-Meyer) and there-

*Among available models we found: Gaussian, Box, Lagrangian, Eulerian, Integral, Computational Fluid Dynamics

fore focus mainly on the highly compressible region close to the jet exit, overlooking the dispersion in the far field Franquet, Erwin and Perrier, Vincent and Gibout, Stéphane and Bruel, Pascal (2015). A complete experimental dataset characterizing the dispersion phenomena of such jets, at ambient or higher temperature, both in velocity and concentration, when submitted to an ABL is still missing.

Promising results via a Particle Image Velocimetry (PIV) and a Mie-Scattering combination measurement technique have already been obtained in terms of velocity and concentration C. Fouchier (2020); Meyer et al. (2007); Chauveau et al. (2006); Price (2022); Beresh et al. (2005). However, such measurements deal with a uniform low-speed cross-flow, conditions often far from mimicking an ABL-like case scenario. Mie-Scattering based technique allows the extrapolation of a relative concentration field C. Fouchier (2020); Karthick et al. (2016) by assuming that, under certain conditions Bohren & Huffman (2008); Hulst & van de Hulst (1981), the light scattered by particles within a specific volume is proportional to the number of particles within this volume. It is a non-intrusive and relatively cost-effective technique that utilizes the same experimental images obtained by the PIV measurements. The combination of PIV and Mie-Scattering results in a non-intrusive optical diagnostic technique requiring the seed material to uniform itself to the fluid flow easily. At high-speed flow conditions, the goodness of the seeding relies on the particle shape (e.g., drag characteristics, consistent scattering cross-section Bohren & Huffman (2008), size), density ratio, materials and ability to overcome agglomeration phenomena (high compressible flows, choking phenomena) Ragni et al. (2011); Scarano (2007).

Absolute non-intrusive concentration measurements are necessary to scale the relative concentration field (pixel intensity). This can be performed using Light Extinction Spectroscopy (LES) measurement, which can provide high-fidelity, relatively localized measurements of the jet concentration in terms of volumetric particle distribution or particle size diameter. The technique relies on measuring the transmittance spectrum of a collimated light beam passing through the particle-laden flow Horváth & Vetrano (2012). The transmitted spectrum can be converted into a volumetric particle size distribution passing through a regularized solution of an ill-conditioned inverse problem I. T. Horváth (2015). This technique has successfully been applied to several types of less severe flows Horváth et al. (2016); Horvath et al. (2016), but rarely similar to the present one Regert et al. (2017). However, a detailed characterization of it in the context of supersonic compressible turbulent flows is still missing.

1.1. Methodology

The present study aims to comprehensively characterize the dispersion of a supersonic underexpanded jet through the analysis of both velocity and concentration fields. A multi-step methodology combining Large-Scale Particle Image Velocimetry (LS-PIV), Mie-scattering theory, and Light Extinction Spectroscopy (LES) is employed to do so.

The goal is to characterize the dispersion close to the release point and in the far-field zone (i.e., the potential core and the self-similar region); the latter experiences a substantial influence of the ABL. To this end, a remarkable field of view (FOV) is required. LS-PIV is, therefore, utilized as the primary technique for a macroscopic velocity field characterization. It extends the measurement region up to $x/D \geq 100$[†] and beyond employing only two cameras. Thus, it makes it possible to cover a range of spatio-temporal scales not only in the radial direction r of the jet but also along the axial one x. After acquiring the LS-PIV campaign's image pairs, Mie-scattering theory is applied to the same dataset to derive a preliminary relative concentration field. Mie-scattering theory allows for the estimation of particle concentration based on the intensity of scattered light. This approach provides an initial characterization of concentration distribution, offering complementary information to the velocity field analysis. However, the concentration map discerned is relative to the maximum pixel intensity registered by the camera sensor.

Light Extinction Spectroscopy lets us obtain a precise and absolute concentration field. It offers direct concentration measurement by quantifying the attenuation of light passing through the jet at a given height x/D. Comparing the light intensity before and after the interaction with the jet can provide accurate concentration profiles, allowing for the calibration and scaling of the relative concentration field derived from the Mie-Scattering theory.

Hence, atmospheric dispersion characteristics analysis comprehensively integrates the velocity and concentration data obtained through LS-PIV, Mie-scattering theory, and LES. The goal is to clarify the relation between flow dynamics and particle dispersion, contributing to improving pollutant mitigation strategies. To this end, different supersonic jets will be investigated without cross-flow. The latter will provide a foundation for successive studies on supersonic jets subjected to an ABL.

1.2. Experimental conditions

The experimental conditions presented herein are designed to investigate the dispersion characteristics of supersonic underexpanded jets discharging into a quiescent atmosphere $U_\infty \approx (0, 0, 0)$. It is essential to note that these conditions do not account here for the influence of the ABL. Instead, the focus is on understanding the fundamental behavior of the jet in an unconfined environment. Also, the decision to exclude the influence of the ABL is deliberate as it stems from the necessity to develop and refine the three essential measurement techniques: LS-PIV, LES, and Mie-Scattering. By simplifying the experimental setup to a jet discharging into the atmosphere without the complexities introduced by the ABL, we aim to establish a solid foundation for applying these methodologies in conjunction with an ABL.

Three distinct upstream total pressure p_0 levels within the tank have been tested: 5, 7, and 9 $[bar]$.

[†] $x =$ axial direction, $D =$ nozzle orifice diameter

The total temperature T_0 inside the tank depends directly on the ambient and compressed air temperature at which the source tank is located outside the von Karman Institute. The only temperature modifications induced are due to the compression and expansion processes during the test procedure. The p_0 range tested offers insights into the jet's response to changes in upstream conditions. Indeed, the choice of pressure values is not casual. Recalling the isentropic relations linked to the Prandtl-Meyer expansion theory, we could predict the severity of underexpansion. To do so, first, we need to predict the pressure right at the nozzle exit in sonic condition ($Ma \approx 1$)

$$\frac{p_e}{p_0} = \left(\frac{2}{\gamma+1}\right)^{\frac{\gamma}{\gamma-1}} \tag{1}$$

Later on, by introducing the *nozzle pressure ratio* η_N, a non-dimensional parameter that relates the static pressure at the nozzle exit p_e to that one of the ambient in which the jet discharge p_∞, it is possible to locate the three expansions initiated by the release into the atmosphere:

$$\eta_N = p_e/p_\infty \tag{2}$$

- *week underexpansion:* it usually describe a jet characterize by $1.1 \geq \eta_N \geq 2.5$. The potential core structure is dominated by the interaction and reflection of the shockwaves along the jet meanline; a *diamond* pattern usually appears.
- *moderate-to-high underexpansion:* the increase of pressure ratio (i.e., the nozzle pressure ratio), $2.5 \geq \eta_N \geq 4$, causes the intersection of the shock waves to no longer lie on the axis of symmetry. A Mach disk is established: the height and position of it are defined by the two symmetric triple points.‡. A series of shock cells appear, each defined by the position of the Mach disks.
- *strong underexpansion:* a further increase of the upstream pressure, such that $\eta_N \geq 4$, decreased the number of shock cells to a point where only a curved Mach disk is present. No other reflection appears downstream of it.

A similar non-dimensional quantity relating to the upstream total pressure p_0: the *jet pressure ratio* η_J, which describes the upstream total pressure to the ambient in which the jet discharge p_∞.

$$\eta_J = p_0/p_\infty \tag{3}$$

Further insights into how the potential-core structure has evolved in parallel with the increase in pressure is reported in Franquet, Erwin and Perrier, Vincent and Gibout, Stéphane and Bruel, Pascal (2015). The following table summarizes the previous quantities:

‡The triple point corresponds to a region where the oblique, intercepting, and reflecting shocks meet

Table 1. Test conditions investigated.

p_0 Pa	p_e Pa	T_0 K	T_∞ K	η_N [-]	η_J [-]
500000	264141	≈ 288.15	≈ 293.15	2.61	5
700000	369797	≈ 288.15	≈ 293.15	3.65	7
900000	475474	≈ 288.15	≈ 293.15	4.69	9

2. Large-Scale Particle Image Velocimetry

Particle Image Velocimetry has emerged as one of the most essential non-intrusive optical techniques, elevating the understanding of the physics that shapes our planet. The ability to provide high-fidelity data is often directly related to the spatial and (or) temporal resolution achievable within the available instrumentation. Consequently, investigations are expected to be conducted over FOV limited to a few square millimeters to maximize the information obtainable given a fixed number of points (camera resolution). The primary purpose of Large-scale Particle Image Velocimetry is to overcome these limitations by dealing with FOVs that can be even two orders of magnitude more significant than the conventional one. Indeed, it becomes essential in cases where the goal is to describe large-scale phenomena, such as the spread of high-speed jets into the atmosphere under the influence of an ABL.

2.1. Experimental setup

The experimental setup is composed of a vertical cylindrical pressurized stainless-steel tank with a $100\ [l]$ (liter) capacity. A $40\ [cm] - 1/2"\ [in]$ pipe is installed at the upper access point within the tank; at the end of it, a $D = 5\ [mm]$ orifice nozzle is mounted. A solenoid valve lets an instantaneous, on-demand jet release before the vertical pipe.

The experiments are performed in a quiescent environment with no cross-flow. The light source utilized for the measurement plane illumination comes from a double cavity pulsed $200\ [mJ/pulse]$ Nd:Yag laser. A plano-convex spherical lens is first used to reduce the beam diameter from the laser source. Later, a plano-convex spherical lens $f = 1003.5\ mm$ and a cylindrical one shape the laser beam into approximately a $1.5 - 2\ [mm]$ thick sheet. A prism is used to deviate the laser sheet coming from the top-left corner. Medicinal mineral white oil *Shell Ondina X 420* (refractive index at $20°$ equal to $n = 1.454$)[§] is used to seed the flow via a Laskin nozzles-based seeding generator. The image acquisition system is composed of a single high-resolution camera equipped with a sCMOS sensor Imager SX 4M CamLink from *LaVision*, $5.5\ [\mu m]$ pixel size, 2360×1776 pixel resolution, 16

[§]Value taken from supplier's technical data sheets

bits quantization provided with a $35mm$ focal-length lens mounted in portrait mode and operating in double-frame mode. A third-order polynomial was used in the calibration process in addition to a calibration verification to ensure the overlap of the laser light sheet plane over the calibration plate. Measurements are performed in the plane of symmetry, along the jet meanline, over a region extending in the range $4 \geq x/D \geq 54$ along the axial direction and $-19 \geq r/D \geq 19$ in the radial spreading direction. It leads so to a (190×250) $[mm]$ (w x h) FOV[¶]. A total of 600 image pairs have been acquired per test. A non-reflective dark background was placed right after the jet to minimize light reflections and to have a uniform background reference field. A setup schematic can be found in Fig.2.

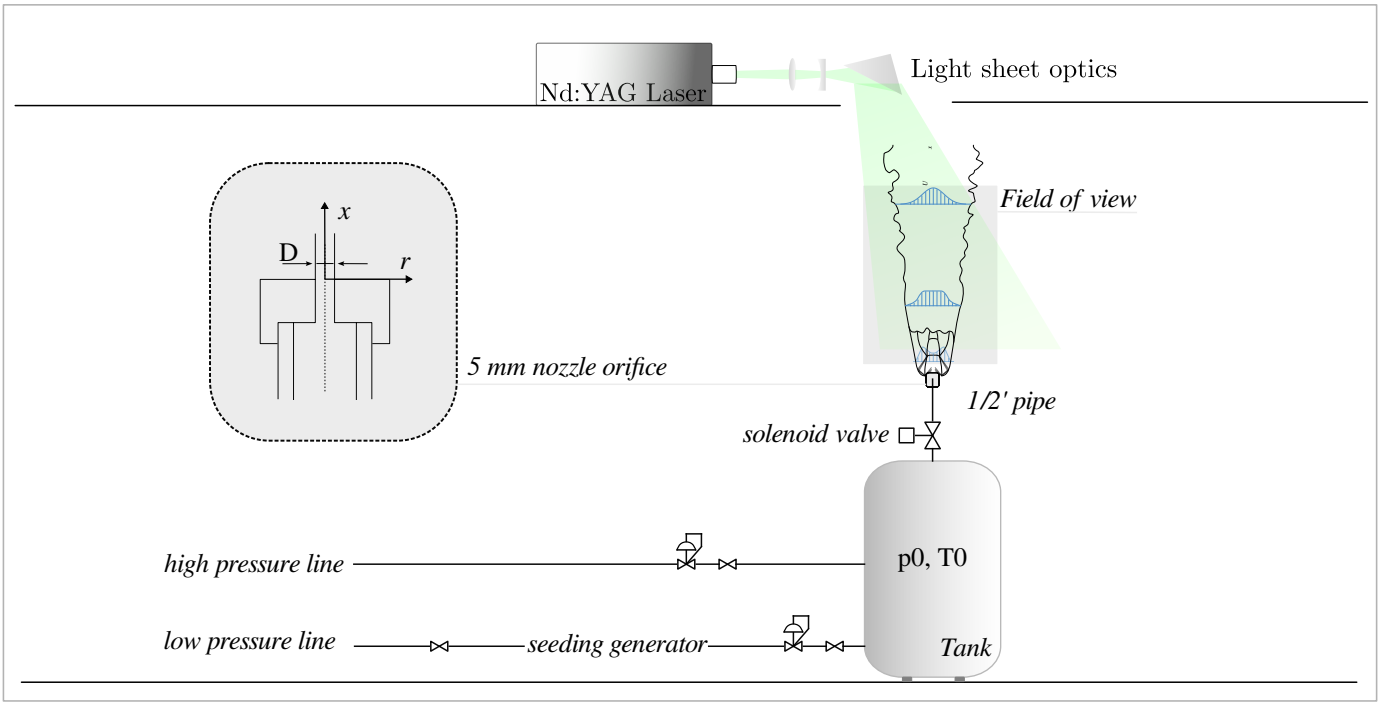

Figure 2. Large-Scale Particle Image Velocimetry setup.

Expected highest velocity magnitude for the $\eta_n = 2.61$ case are in the order of $U_e \approx 300$ $[ms^{-1}]$ while almost $U_e \approx 500$ $[ms^{-1}]$ for the $\eta_N = 4.69$. The previous reference values come from the dispersion study conducted in C. Fouchier (2020). Typical separation time between the two laser pulses of the order of $\delta_t = 1$ $[\mu s]$ has been chosen to obtain an average pixel displacement of about 8 pixels in the region close to the potential core (here the highest velocities are expected). In the far-field zone, the self-similar region $x/D \geq 15 - 20$, velocities of an order of magnitude less are expected: different tests varying the pulse separation time up to $\delta_t = 10$ $[\mu s]$ are conducted to keep the pixel displacement within the previously mentioned value.

[¶]FOV = Field Of View

2.2. Data post-processing and validation

The classical and well-established iterative multi-grid cross-correlation (MGCC) Westerweel et al. (1997); Scarano & Riethmuller (1999); Stamhuis & Thielicke (2014) approach has been selected as the first step towards extrapolating the velocity fields. An initial 64×64 interrogation window with 50% overlapping was chosen, followed by a 32×32 pixel in step 2 up to a final 16×16 interrogation window size for the third and last step. The latter lead to a spatial resolution of $\approx 1.72 \times 10^{-3}$ $[m]$ in the axial direction while $\approx 1.73 \times 10^{-3}$ $[m]$ along the cross-stream.

It is widely understood that the maximum spatial resolution is directly linked to the size of the last interrogation window of the MGCC iterative procedure Scarano (2003); Raffel et al. (2018). However, as the number of particle images per interrogation window is decreased, the information is reduced and the result is more likely to be affected by random correlation peaks, lower S/N[||] and/or random errors in sub-pixel peak interpolation Scarano (2001); Raffel et al. (2018); Keane & Adrian (1989); Prasad et al. (1992). Consequently, a wider interrogation window is both more robust and, when the velocity gradient is relatively small, such as in the self-similar region (see Fig. 1), can also provide a more accurate sub-pixel displacement interpolation. On the other hand, if the length scale of the velocity fluctuations is smaller than the interrogation window, such as at the jet edges in the self-similar region, the interrogation could perform poorly. It also follows that the size of the interrogation window is indeed limited by the average particle spacing: a high seeding density is desirable to achieve a lower spatial wavelength cut-off. Since the 16^2 px interrogation size has been adopted as the last step for the entire field and given the consequent spatial resolution of $\approx 2 \times 10^{-3}$ $[m]$, we expect to reach good accuracy both quantitatively and qualitatively right after the potential core, from the transition up to the self-similar region. In that region, indeed, a higher resolution is required because of the presence of the strongest gradient in both the spatial directions due to the reflections and interactions of the shocks Elsinga et al. (2005); Scarano (2003). As already mentioned, the displacement of the seeding particles is exposed to the shear layer, motion blur due to the presence of the shocks and maybe an excessive seeding density because of the lower radial spreading of the jet or simply a too-high seeding density. All of the previous makes the peak displacement shape became more elliptical. For this purpose, a $2 - D$ Gaussian function approach Nobach & Honkanen (2005) with a 9-point fit has been selected for the sub-pixel interpolation procedure instead of a classical 3-point fit Gaussian approach. In order to increase even more the robustness of the cross-correlation, a post-validation procedure based on Hart (2000) has been added. The goal of this is to reduce outlier vectors that may result from a bad cross-correlation map. It consists of repeating the cross-correlation four times more, for each of the cross-correlation maps obtained at the end of the MGCC procedure: the original interrogation windows are shifted by a desired, relatively small ($10 - to - 25\%$), step towards the positive and negative x and y direction. Results are multiplied leading to a final cross-correlation map where

[||] Signal-to-noise ratio

spurious displacements that are not present in each of the resulting five maps are penalized.

Estimating statistical flow quantities usually requires a certain number of valid samples. Statistically, for a given dataset (i.e., a subset of every possible observation), we define the arithmetic pixel displacement sample mean $\Delta\bar{x}_i$ as

$$\Delta\bar{x} = \frac{1}{N}\left(\sum_{i=1}^{N}\Delta x_i\right) \tag{4}$$

where Δx_i and $\Delta\bar{x}$ represent a pixel displacement single measurement, and the corresponding mean value, N, is the number of samples; the procedure is controlled by the variable i. Each test is made of $N = 600$ image pair; however, the convergence of the $\Delta\bar{x}$ is reached approximately after 150 image pairs. It is worth recalling that every measurement of a variable x consists of its real value $\tilde{x}$ plus an error ϵ

$$x = \tilde{x} + \epsilon \tag{5}$$

Random errors are non-predictable, even in magnitude or sign. The standard deviation of the error σ_X defined as has been used to determine the precision of the measurements.

$$\sigma_{\Delta x} = \sqrt{\frac{1}{N-1}\sum_{i=1}^{N}(\Delta x_i - \Delta\bar{x})^2} \tag{6}$$

The measured $\sigma_{\Delta x}$ has been checked at different locations along the jet ($x_1/D = 10$, $x_2/D = 20$, $x_3/D = 30$, $x_4/D = 40$) and convergence has been reached for each of the them around a value of $\sigma_{\Delta x} = 0.02$ px outside the potential core, in the selfsimilar region. However, peaks around $\sigma_{\Delta x} = 0.15$ px, up to a maximum of $\sigma_{\Delta x} = 0.4$ px, have been found inside the potential core. We attribute this difference mostly to low spatial resolution available to describe correctly the strong gradients established by the presence of the shock waves.

2.3. Results

In Fig. 3, the decaying of the mean axial velocity as the increasing of x/D is reported. The trend refers to $\eta_N = 3.65$ corresponding to an upstream tank total pressure of 7 $[bar]$ ($\eta_J = 7$). Also, the increasing radial spread of the jet as moving far from the exit is appreciable.

After the transition region, which links the potential core to the far-field zone, the profiles of Fig. 3a plotted against ζ collapse into a single curve as shown in Fig. 3b. The non-dimensional parameter ζ is defined as the ratio of the radial position r which starts from $r = 0$ (meanline), over the position $r_{1/2}$, i.e. where velocity U_r is equal to half of the maximum velocity $1/2U_0$ (on the meanline) at that given x/D, refer to Pope (2001) for an extended treatment of the topic. The previous trends

defined in Fig. 3a and Fig. 3b have been found for each of the pressures tested, confirming so to be independent of the local Reynolds number here defined as $Re_0(x) = r_{1/2}U_0(x)/\nu$ Pope (2001).

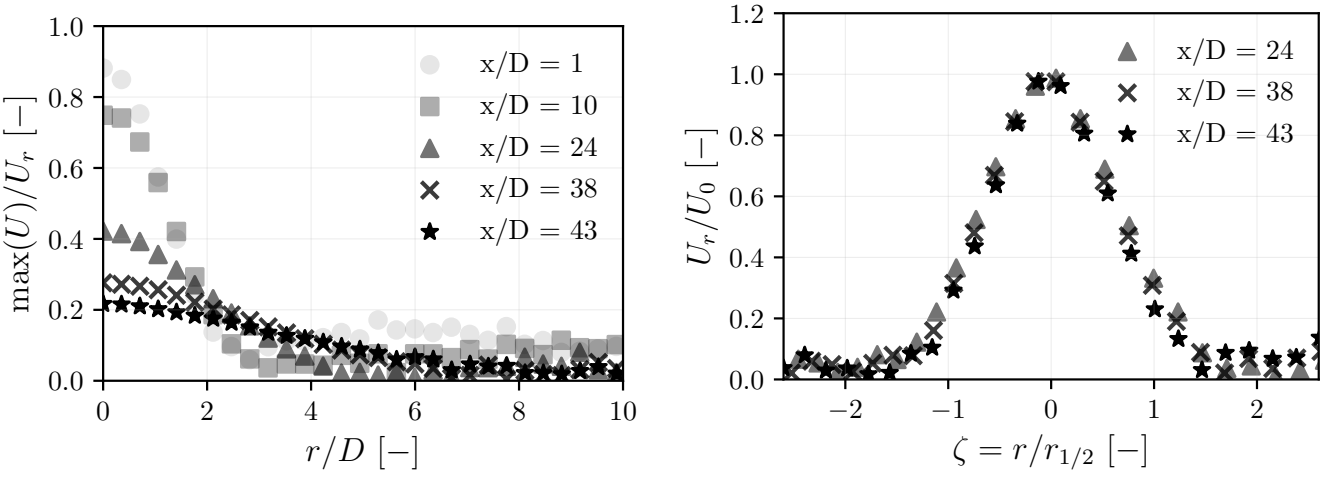

(a) (b)

Figure 3. (a) Radial profiles of non-dimensional mean axial velocity in a supersonic *moderate-to-high* underexpanded jet ($\eta_N = 3.65\ [-],\ p0 = 7\ [bar]$) discharging in a calm atmosphere. (b) Mean axial velocity profiles of a supersonic *moderate-to-high* underexpanded jet ($\eta_N = 3.65\ [-],\ p0 = 7\ [bar]$) collapsing onto a single curve within the self-similar region.

The classical multi-grid cross-correlation (MGCC) approach, despite detecting acceptable velocity magnitude, starts to suffer when there is the need to rely on a cross-correlation map-based data validation. The inherent uncertainties derived from the strong velocities gradient, the large FOV, out-of-plane motion, lower spatial resolution, and potential artifacts associated with the cross-correlation technique raise concerns about the accuracy and reliability of the obtained results. To address these limitations, but mainly to validate the results obtained via the MGCC approach, it has been decided to check the effect of averaging the single cross-correlation maps instead over the same set of images rather than averaging the extracted peak displacement vectors Willert (2008). The approach is called ensemble cross-correlation and it was initially developed for micro-fluid PIV Santiago et al. (1998); Westerweel et al. (2004). Indeed, the ensemble cross-correlation approach revealed consistent pixel displacements across different realizations, lending up to now greater confidence in our results Kähler & Scholz (2006). Specifically, we observed that the absolute mean difference peaks along the mean line between successive frames were found to be approximately 0.2 pixels per frame. Those values, which are located again inside the potential core, are close to the values of $\sigma_{\Delta x}$ previously defined. Outside the potential core one order of magnitude less has been found, in good agreement with the previous 4 points mentioned. The actual shape of the cross-correlation maps and the resulting values of S/N made the results obtained through the MGCC algorithm fall within reasonably acceptable values, as can be clearly appreciated in Fig. 4a.

To conclude, the jet mean axial velocity profiles have been reported for each of the three pressures tested in Fig. 4b.

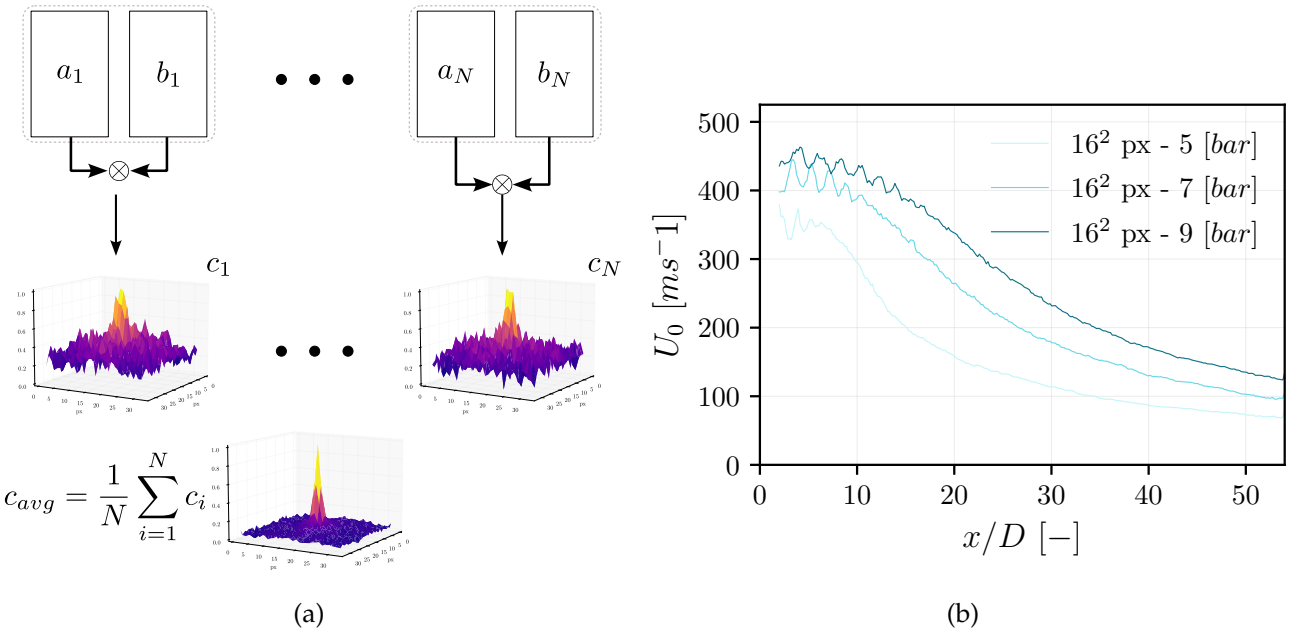

(a) (b)

Figure 4. (a) Principle of the ensemble cross-correlation approach applied to the $\eta_J = 7$ test case. The smoothing effect and the clear peak detection are appreciable in the resulting averaged cross-correlation map c_{avg}. (b) Mean axial velocity profiles for the three different pressures tested.

2.4. From PIV to Mie-Scattering: measuring a relative concentration

The jet dispersion concentration field is derived using a Mie-Scattering theory-based technique, which operates on each single pixel intensity of the gray-scale experimental images. The Mie-Scattering technique assumes that, in some conditions, the light scattered by a cloud of particles is proportional to the number of particles within this cloud Hulst & van de Hulst (1981); Bohren & Huffman (2008).

For this purpose, the following assumptions have been made:

- The incident light is a plane monochromatic electromagnetic wave.
- Particles are homogeneous mono-dispersed spheres.
- The particle number density is small enough within the measurement volume to consider single scattering phenomena.

The technique has the main advantage of being non-intrusive and operates on the same set of image pairs acquired by the LS-PIV campaigns; therefore, a simultaneous measurement of velocity

and concentration can be achieved. In addition, the entire FOV coming from the LS-PIV can be used to describe the concentration instead of a single spatial point typical of a probe measurement.

The scattered signal R of a particle could be expressed as:

$$R = K_s C I \tag{7}$$

where K_s represents the efficiency of the optical system in retrieving R, the concentration of particles within the pixel volume C and the incident light from the laser sheet I Hulst & van de Hulst (1981). A simplified schematic view of the phenomenon is shown below:

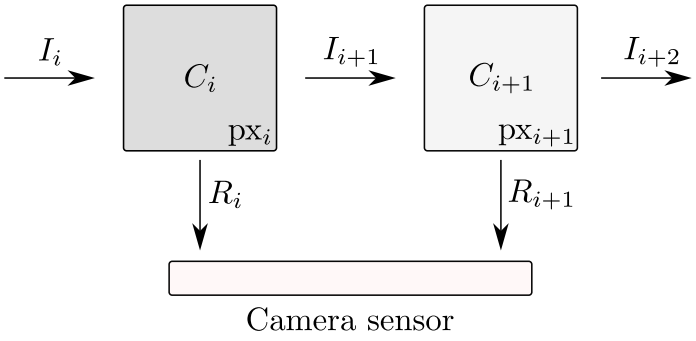

Figure 5. Light incident and scattered by two consecutive pixel volume of N particles giving a concentration C_i

The problematic part is linked to the definition of optical efficiency K_s. This is usually done by calibrating the system using a known absolute value of C from a reference area. The latter is precisely our unknown and desired parameter to be measured. However, a relative value C_{rel} can still be measured without knowing the efficiency K_s. This is done by recording a reference value of the light scattered R_{ref} using the same experimental condition (i.e., the incident light I needs to be the same and indeed the K_s too). So, by relating the latter measurement with the actual concentration measurement of a jet, it is possible to extract a relative concentration map:

$$C_{rel} = \frac{C}{C_{ref}} = \frac{R}{K_s I}\frac{K_s I}{R_{ref}} = \frac{R}{R_{ref}} \tag{8}$$

The laser reflections and the background light could lead to the presence of artifacts in the concentration map. These can be solved by acquiring calibration images and then averaging them to obtain a mean background light distribution I_{BL}. Experimentally, it is acquired by simply switching on the laser source and starting the acquisition of the ambient unseeded. The resulting map is later subtracted from the jet concentration measurement intensity I and the reference one I_{BS}. The latter is acquired by uniformly seeding the FOV with the same seeding particles used to seed the supersonic jet and likewise illuminated by the same laser intensity source utilized for visualizing the jet. Examples of the previous are reported in Fig.**??**

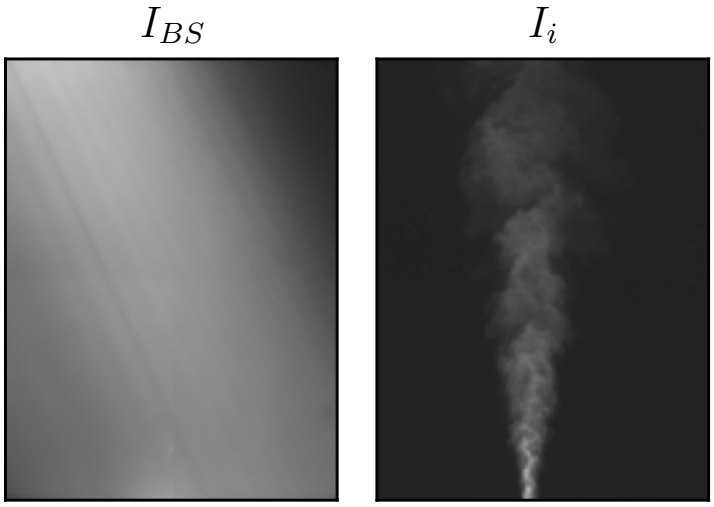

All the ingredients to derive a C_{rel} are ready

$$C_{rel} = \frac{I - I_{BL}}{I_{BS} - I_{BL}} \tag{9}$$

To facilitate the reading of the resulting map, and so the concentration distribution, C_{rel} is scaled in the $[0, 1]$ range using the maximum value recorded I_{ref} by Eq. 9: $C_{rel} = max(C_{rel})^{-1} C_{rel}$ In Fig. 6, the relative concentration maps from Eq. 9 have been reported. 600 samples have been averaged (1 test) for each of the quantities in Eq. 9.

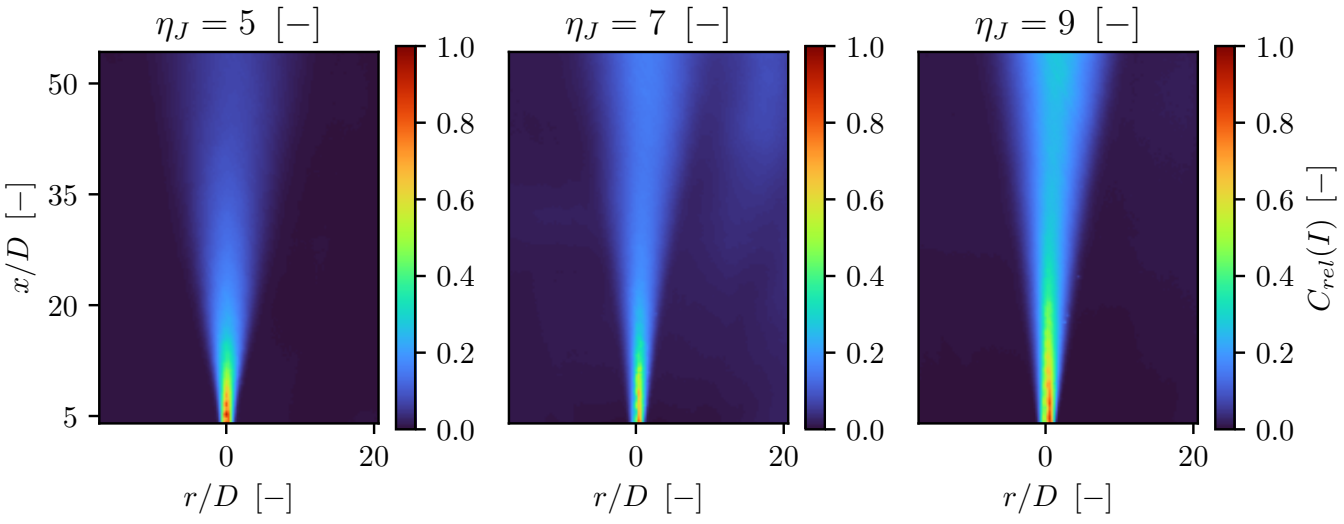

Figure 6. Relative concentration fields for the three different pressure ratios tested.

3. Light extinction spectroscopy

The objective here is to employ an experimental methodology aimed at quantifying the size and number of particles within a precise region of a supersonic underexpanded jet discharging into the atmosphere. Consequently, the results from the measurement will be used to scale the relative concentration maps (see Fig.6) obtained from the Mie-Scattering theory. At this end, Light Extinction Spectroscopy offers a non-intrusive means of assessing particle characteristics by analyzing their light transmission spectra within the Ultraviolet-Visible-Near-Infrared (UV-VIS-NIR) spectrum.

3.1. From light to concentration: an absolute measure

In nature, extinction cannot be directly quantified. Instead, the effects of absorption and scattering are taken into account by recording the transmittance $T(\lambda)$, which is defined by the ratio of the light outgoing the solution I by the total incident light entering the solution I_0 Hulst & van de Hulst (1981).

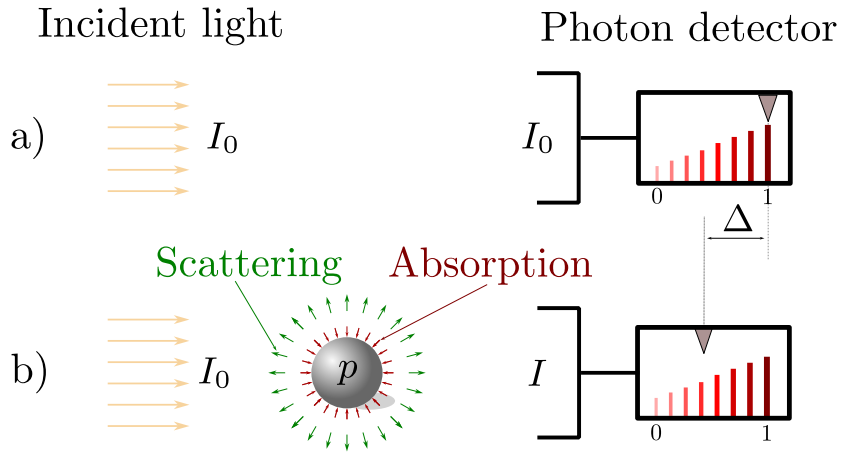

Figure 7. Principle of the light *extinction* process.

By taking into account the *Beer-Lambert* law, we can reformulate it considering the exponential decrease with the attenuation coefficient τ and the path length covered by the light beam L:

$$T(\lambda) = \frac{I}{I_0} = \exp(-\tau L) \tag{10}$$

Regarding the scattering phenomenon occurring within a supersonic underexpanded jet, the following simplifying assumptions are made herein:

- The scattering is elastic.
- The scattering is independent.

- Single spherical particles cause the scattering.

Based on these assumptions, the attenuation coefficient of the particle ensemble can be written as:

$$\tau = \sum_i N_i C_{ext,i} \tag{11}$$

Since $T(\lambda)$ is a dimensionless quantity, τ needs to have a dimension of $[1/m]$ representing the attenuation coefficient per unit path length $[m]$. Consequently, N_i is the total number of particles per unit volume of type i while $C_{ext,i}$ is the correspondent extinction cross-section of the $i-th$ particles type. Substituting Eq. 11 in Eq. 10 and replacing the summation with the integral within the desired particles size range $D_{min} \leq D \leq D_{max}$ we approach the final form of the problem.

$$\int_{D_{min}}^{D_{max}} C_{ext}(m, \lambda, D) N(D) dD = -\frac{1}{L} ln T(\lambda) \tag{12}$$

The introduction of a more general definition of the particle scattering property through the definition of the extinction matrix Q_{ext} Hulst & van de Hulst (1981), which relates the cross-sections C_{ext} to the geometrical cross-section of the particle, allows the definition of the dimensionless scattering efficiency factors. With the aid of some basic math and by defining a volumetric PSD** function $V(D)$ is it possible to adjust Eq. 11 into finally

$$\int_{D_{min}}^{D_{max}} Q_{ext}(m, \lambda, D) \frac{V(D)}{D} dD = -\frac{2}{3} L ln T(\lambda) \tag{13}$$

Hence, the volumetric PSD function on the left-hand side $V(D)$ could be discretized into n_i particle diameters as the $T(\lambda)$ on the right-hand side into n_λ points among the wavelength range of interest. The latter is usually directly determined by the resolution of the instrumentation used.

3.2. Experimental setup

From the experimental side, the technique relies on acquiring the transmittance spectrum $T(\lambda)$ of a light beam passing through the measurement region of interest. The instrumentation required consists of a Deuterium-Tungsten Halogen UV-VIS-NIR electromagnetic light source emitting a divergent light beam towards a 90°off-axis parabolic mirror. Off-axis parabolic mirrors are mirrors whose reflective surfaces are segments of a parent paraboloid. It achromatically collimates and deviates by 90°the initially divergent electromagnetic beam source into the jet; the off-axis design separates the focal point from the rest of the beam path. The parabolic surface has a UV-enhanced aluminum coating that increases the reflectance properties within the range of interest.

**Particle Size Distribution

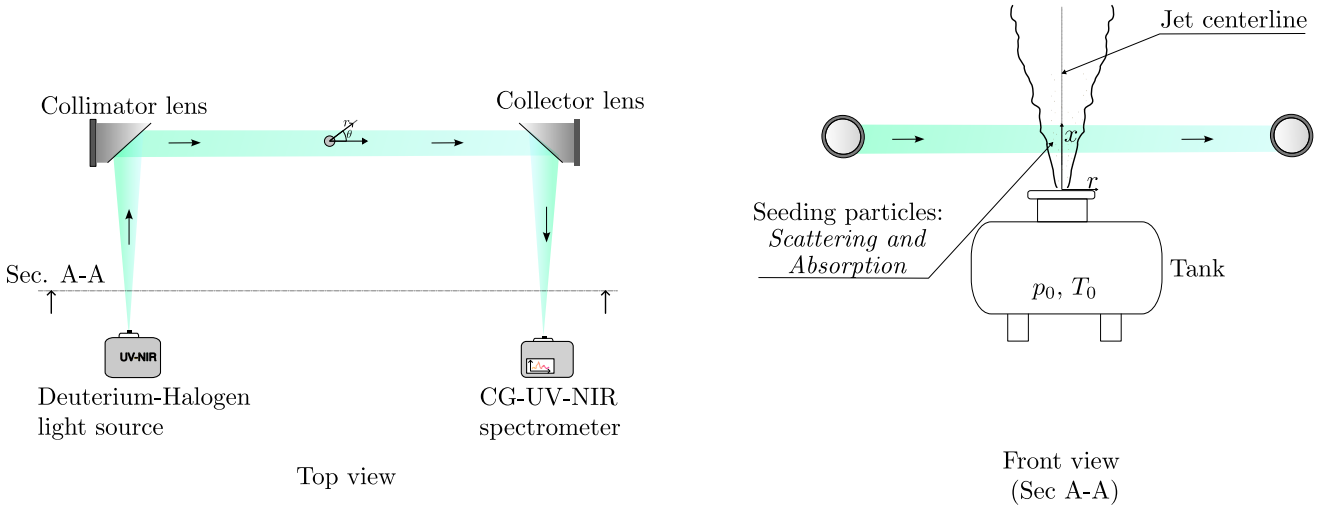

Figure 8. Experimental setup for the light Extinction spectroscopy.

Consequently, the resulting attenuated $light$[††] beam goes into a collector mirror, identical to the previous one, which focuses it into a composite grating high-resolution miniature fiber optic spectrometer also operating in the UV-VIS-NIR range spectrum. It provides optical resolution as good as 0.025 $[nm]$ (FWHM[‡‡]) being responsive within $200 - 1100$ $[nm]$ wavelength range. The CCD silicon-based linear array photo-detector has a resolution of 3648 pixels. Each spectrum acquired consists of 3648 values along the wavelength range considered (typically $200 - 1100$ $[nm]$ in the present study). The specific range and resolution also depends on grating and entrance slit selections. The experimental setup is straightforward to prepare; the main concern, on the other hand, as usually required in optical measurement techniques, lies in precisely aligning and mounting the two off-axis parabolic mirrors. This phase is crucial as it ensures minimal light loss and accurate full-scale range measurements.

A typical test is performed by recording the spectrum of the previously defined light beam traveling through the particles dispersed into the supersonic jet $S(\lambda)$ and comparing it to a reference spectrum $S_{ref}(\lambda)$. However, the signal seen by the spectrometer is a summation of the signal caused by the light source (e.g., $S(\lambda)$, $S_{ref}(\lambda)$) and noise coming from external inevitable illumination of the ambient or noise inherent the instrument $D(\lambda)$.

The measurement starts with acquiring the background noise $D(\lambda)$ by removing the light from the spectrometer. Then, the reference spectrum $S_{ref}(\lambda)$ can be acquired by simply turning on the light source. At this point, the test could be performed by acquiring the spectrum of interest by triggering the release of the seeded jet. Hence, the correct transmittance spectrum $T(\lambda)$ is obtained

[††] Rigorously intended as electromagnetic radiation in the UV-NIR wavelength range, so not *simple* visible light.

[‡‡] The spectral resolution of a spectrometer is defined as the wavelength of the light being measured divided by the full-width half maximum (FWHM) of the spectral peak being investigated.

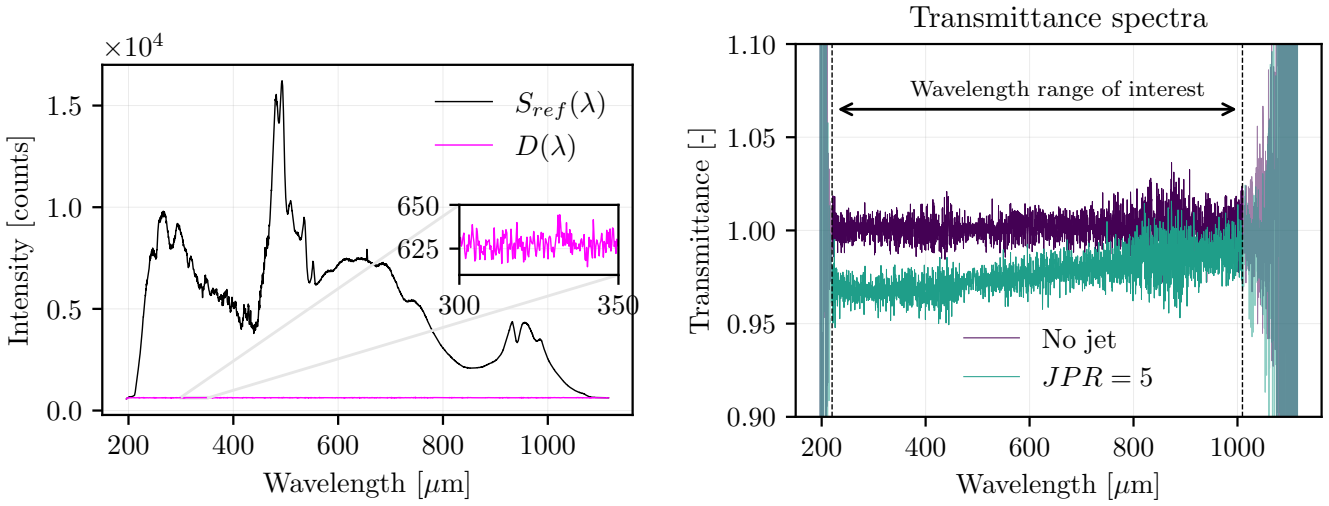

Figure 9. (a) Reference $S_{ref}(\lambda)$ and dark $S(\lambda)$ spectrum spectrum used to derive the transmittance spectrum from Eq. 14. (b) Comparison of the transmittance spectra before (*No jet*) and after releasing the jet ($JPR = 5$)

$$T(\lambda) = \frac{S(\lambda) - D(\lambda)}{S_{ref}(\lambda) - D(\lambda)} \tag{14}$$

The goal behind measuring $T(\lambda)$ is to obtain PSD information within the measurement volume. The latter will be used as the main ingredient in obtaining the solution of an inhomogeneous Fredholm integral equation of the first kind (Eq. 13) is demanded. The latter can also be seen as:

$$g(t) = \int_a^b K(t,s) f(s) ds \tag{15}$$

The tricky part concerns the kernel function $K(t,s)$ (i.e., the extinction matrix $Q_{ext}(m,\lambda,D)$). Indeed, it has a solid and undesired smoothing effect; therefore, significant changes in $f(s)$ (i.e., the volumetric PSD) are represented by minimal changes in the transmittance spectrum $g(t)$. Thus, small random disturbances in $g(t)$ should arise from significant corresponding changes in $f(s)$. In the same way, minor measurement errors in $g(t)$ lead to nonphysical and often oscillatory values of $f(s)$. Several ways exist to overcome the above problem. The central idea is to find a robust, unique correspondence between $g(t)$ and $f(s)$ even at the cost of losing some details of the underlying $f(s)$. The chosen method is taken from I. T. Horváth (2015); Horvath et al. (2016) where existing numerical techniques have been combined, focusing on reliability and accuracy. Specifically, it is a direct, non-negative, optimized Phillips-Twomey regularization I. T. Horváth (2015).

3.3. Absolute concentration results

As a result of the inversion, one can extrapolate from $T(\lambda)$ absolute precise concentration quantities such as a volumetric PSD function showed in Fig. 10a or the number of particles per cubic meter within a specific size as in Fig. 10b. The imposed size range has been divided into 100 sizes among $D_{min} = 1000\ [nm]$ and $D_{ma} = 10000\ [nm]$ to match the particle seeding generator's capabilities and large enough also to include bigger particles formed by the agglomeration phenomena that arise in high-speed compressible flows.

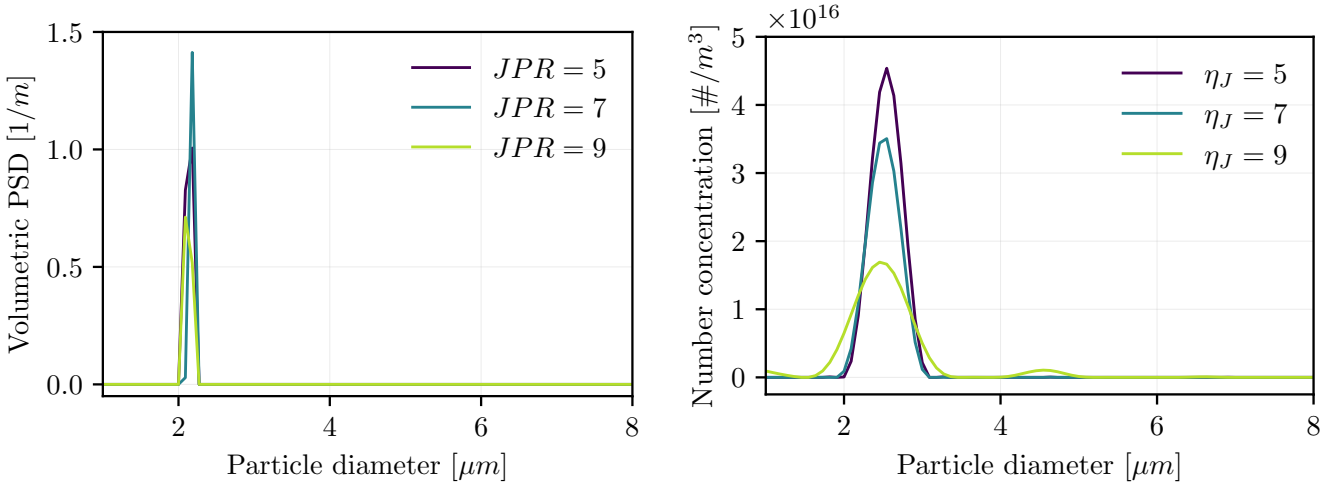

Figure 10. (a) Volumetric PSD function within the measurement volume obtained with a 2^{nd} order accuracy. (b) Particle size distribution within the measurement volume obtained with a 2^{nd} order accuracy.

The present results refer to a measure made at $x/D = 10$. The path length of the light beam (see Fig. 8) is equal to $l_p = 0.0925\ [m]$, and the diameter of the beam is equal to $d_b = 0.0075\ [m]$. The path length and the beam diameter could be used to derive the cylindrical measurement volume. Further quantities could be derived, such as the total volume occupied by the particles within the measurement volume (see Fig. 11a) and the total number of particles of various sizes within the measurement volume for each of the tested pressures (see Fig. 11b). Preliminary results obtained with a 0^{th} order of accuracy implementation (based on the Singular Value Decomposition) of the algorithm have also been plotted. The inversion almost perfectly matched the volume fraction occupied by the total number of particles using a 0^{th} and 2^{nd} order (based on the Generalized Singular Value Decomposition) of accuracy. However, it jumps out how the 0^{th} order tends to detect a lower total number of particles per unit volume, suggesting the tendency to detect a more significant number of particles having bigger diameters. It should be noted that the concentration of the jet at a given height is inversely proportional to the upstream tank total pressure. The latter, as already stated, describes the severity of *underexpansion* of the supersonic jet.

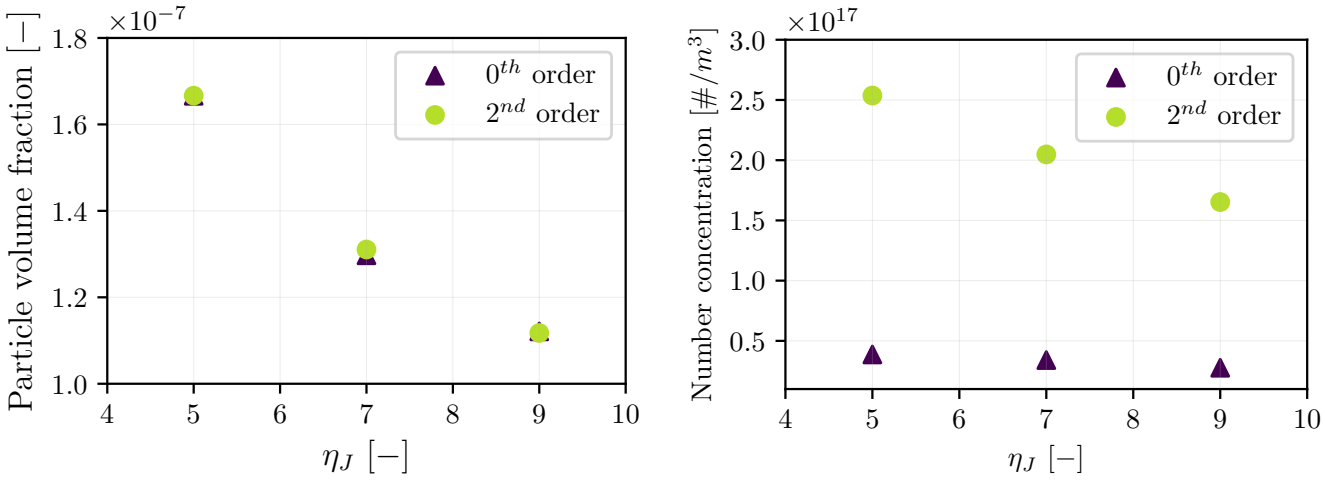

(a) (b)

Figure 11. (a) Total volume fraction occupied by the particles detected within the measurement volume. It has been derived by integrating the volumetric PSD obtained in Fig.10a along the imposed particle size range ($1000 \leq D \leq 10000$ $[nm]$). (b) Total number of particles detected within the measurement volume. It has been obtained from the distribution of Fig.10b.

The LES measurements were performed at the same height for each pressure tested. However, we expect the length of the potential core not to be the same for each of the pressures tested; specifically, a longer length is anticipated as the pressure ratio increases. Almost certainly, the size is higher than $x/D = 10$, pointing to the strong possibility that the measuring zone of the jet is still under the influence of the shock cells' repeating pattern. New measurements need to be done outside the potential core in the transition region to bypass the impact of a non-uniform flow behavior within the volume of interest. The previous results must be considered preliminary findings in the more comprehensive context of adapting the LES technique to the domain of supersonic compressible flows. The primary goal is to understand the influence of the two mentioned approach and their role in such different total numbers of particle detection previously reported in Fig. 11b. In parallel, the influence of the most relevant parameter during the experimental measure, such as the beam path length l_p, the quality of the beam collimation, the refractive index behavior and its uncertainty related to the compressibility effects in supersonic conditions, particle agglomeration phenomena and later the delicate phenomenon of multiple scattering is still unknown and therefore needs further detailed study.

4. LES-Mie concentration characterization

The relative concentration maps derived through the Mie-Scattering theory for each of the pressure tested, reported in Fig.6 could now be normalized by the absolute concentration values derived

from the inversion of the problem represented by Eq. 13. First, the measurement volume of the LES measurements needs to be defined: it corresponds to a beam having a diameter of $d_B = 0.0075\ [m]$ times the path length of the measurement $l_p = 0.0925\ [m]$. This volume needs to be reduced and precisely matched to the one highlighted by the laser sheet. After this, the matrix portion corresponding to the LES measurement volume is extracted from the relative concentration map and scaled in the $[0, 1]$ range. Later, the total number of particles reported in Fig.11 needs to be spread within the previously defined portion of the matrix. To conclude, the entire FOV is scaled starting from the portion of the matrix just scaled with the absolute concentration value. Finally, C_{rel} can now be updated in Fig 12

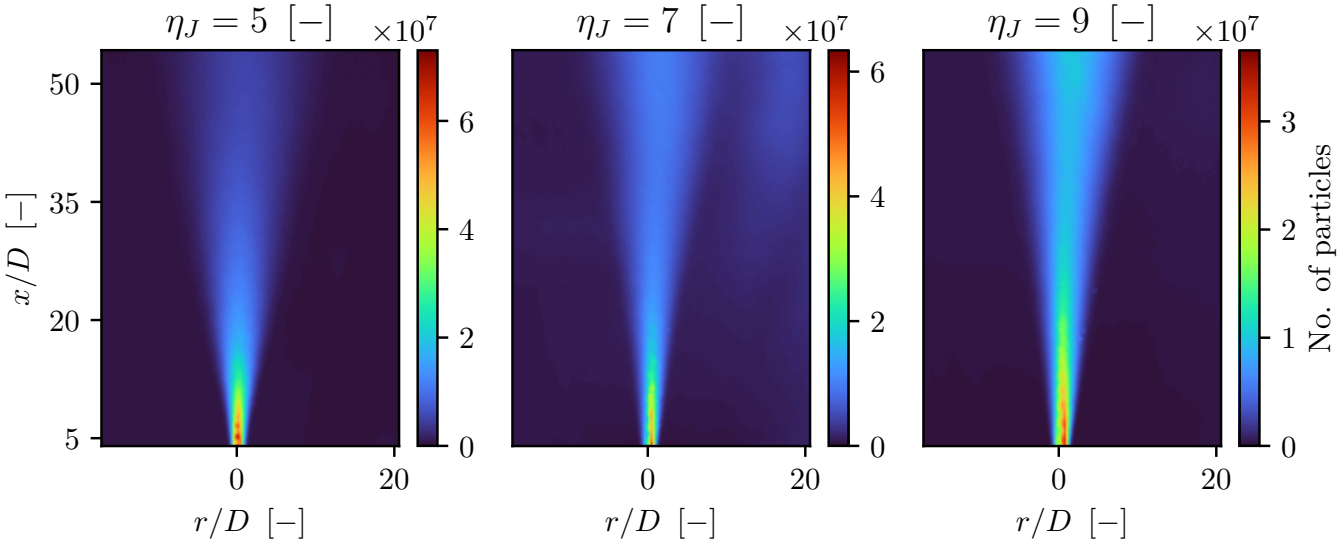

Figure 12. Absolute concentration fields for different jet pressure ratio (η_J) obtained from scaling the relative one with the reference values from the LES measurements. The reader may notice asymmetries in the potential core field distributions for the 7 and 9 bar pressure cases. The latter are due to the pressure sensor upstream influence which will be removed in future tests.

5. Conclusion

The present work aims to lay the foundations to characterize the dispersion phenomenon of an underexpanded supersonic jet influenced by an ABL to mimic a leak from a pressurized tank. Specifically, the interest focuses far from the release point in the self-similar region. Focus has been given to velocity and concentration distribution. To do so, three main techniques have been selected: Large-Scale Particle Image Velocimetry, a Mie-Scattering one, and Light Extinction Spectroscopy. Here, an initial characterization in a quiescent ambient has been conducted to focus on the technique response, avoiding the additional influence of an ABL.

LS-PIV was shown to be able to describe the velocity field outside the potential core, starting

from the transition region to the self-similar region. The large FOV required, which results in a limited spatial resolution, allowed us to capture even the strong gradients of the potential core. However, a considerable low-pass filtering effect is present on the magnitude of the peak values that could be detected. As expected, noisy cross-correlation maps may result when dealing with LS-PIV. However, the ensemble cross-correlation approach has been a powerful tool to validate the displacements obtained via a classical iterative multi-grid cross-correlation approach. Testing and integrating the latter in the MGCC approach as a preliminary px displacement estimation tool is ongoing.

The same set of images acquired via the LS-PIV campaign has been used to retrieve a relative concentration map through the Mie-Scattering theory. The latter showed the possibility of linking the pixel intensity recorded by the camera sensor to an ensemble concentration of particles within the pixel itself. Cost-effectiveness and non-intrusiveness made this technique the right candidate for obtaining a qualitatively accurate relative PSD along the acquired FOV.

Light Extinction Spectroscopy has been employed to measure an absolute reference concentration value. Even if at an early stage, the results of the measurements, usually in terms of volumetric PSD or number of particles per cubic meter, have been used to scale the maps obtained from the Mie-Scattering theory, producing an absolute concentration map of the entire FOV acquired during the LS-PIV campaigns.

Further investigation needs to be done to assess the impact of supersonic compressible turbulence on the scattering process, particularly in the context of multiple scattering phenomena; it is evident that there is much more to uncover. Additionally, adapting the inversion algorithm to address the ill-posedness problem needs to be revised to consider the previously mentioned phenomena. These are crucial for enhancing the effectiveness of our concentration measurements and improving our understanding of compressible-turbulence-induced multiple scattering phenomena.

Nomenclature

ABL	Atmospheric Boundary Layer
LS-PIV	Large-Scale Particle Image Velocimetry
LES	Light Extinction Spectroscopy
Px	Pixel [-]
γ	Specific heat ratio [-]
$\Delta\bar{x}$	Mean pixel displacement [px frame^{-1}]
Δx_i	Pixel displacement [px frame^{-1}]
δ_t	Pulse separation time [μs]
η_N	Nozzle pressure ratio [-]
η_J	Jet pressure ratio [-]

$\sigma_{\Delta x}$	RMSerror [-]
c_{avg}	Averaged cross-correlation map
C	Concentration
C_{ref}	Reference concentration
C_{rel}	Relative concentration
D	Nozzle orifice diameter [m]
f	Focal length [m]
I	Incident light intensity [counts]
I_{BL}	Incident background light intensity [counts]
I_{BS}	Incident background smoke light intensity [counts]
K_s	Optical efficiency [-]
Ma	Mach number [-]
N	Total number of samples [-]
n	Refractive index [-]
p_0	Total pressure [Pa]
p_e	Nozzle exit static pressure [Pa]
r	Jet radial spread direction [m]
R	Light scattering signal [counts]
Re	Reynolds number [-]
Re_0	Local Reynolds number [-]
T_0	Total temperature [K]
T_∞	Ambient temperature [K]
U	Velocity [ms^{-1}]
U_∞	Free-stream velocity [ms^{-1}]
U_0	Jet meanline velocity [ms^{-1}]
U_r	Jet radial velocity [ms^{-1}]
x	Jet axial direction [m]

References

Beresh, S. J., Henfling, J. F., Erven, R. J., & Spillers, R. W. (2005). Penetration of a transverse supersonic jet into a subsonic compressible crossflow. *AIAA journal*, *43*(2), 379–389.

Bohren, C. F., & Huffman, D. R. (2008). *Absorption and scattering of light by small particles*. John Wiley & Sons.

C. Fouchier. (2020). *Investigation of the Pollutant Dispersion Driven by a Condensed-Phase Explosion in an Urban Environment* (Unpublished doctoral dissertation). Universite Libre de Bruxelles.

Chauveau, C., Davidenko, D., Sarh, B., Gökalp, I., Avrashkov, V., & Fabre, C. (2006). Piv measurements in an underexpanded hot free jet. In *13th int symp on applications of laser techniques to fluid mechanics* (pp. 26–29).

Cleaver, R., & Edwards, P. (1990). Comparison of an integral model for predicting the dispersion of a turbulent jet in a crossflow with experimental data. *Journal of loss prevention in the process industries*, *3*(1), 91–96.

Elsinga, G. E., van Oudheusden, B. W., & Scarano, F. (2005). The effect of particle image blur on the correlation map and velocity measurement in piv. In *Optical diagnostics* (Vol. 5880, pp. 291–302).

Franquet, Erwin and Perrier, Vincent and Gibout, Stéphane and Bruel, Pascal. (2015). Free underexpanded jets in a quiescent medium: A review. *Progress in Aerospace Sciences*, *77*, 25–53.

Hart, D. P. (2000). Piv error correction. *Experiments in fluids*, *29*(1), 13–22.

Holmes, N. S., & Morawska, L. (2006). A review of dispersion modelling and its application to the dispersion of particles: An overview of different dispersion models available. *Atmospheric environment*, *40*(30), 5902–5928.

Horvath, I. T., Colinet, P., & Vetrano, M. R. (2016). Assessment of the light extinction spectroscopy technique for submicron particle characterization. *Powder technology*, *291*, 375–382.

Horváth, I. T., Colinet, P., & Vetrano, M. R. (2016). Measuring contact angles of small spherical particles at planar fluid interfaces by light extinction. *Applied Physics Letters*, *108*(20).

Horváth, I. T., & Vetrano, M. R. (2012). Development of the multi wavelength light extinction technique for the characterization of nanoparticles–data inversion. In *9th national congress on theoretical and applied mechanics, brussels.*

Hulst, H. C., & van de Hulst, H. C. (1981). *Light scattering by small particles*. Courier Corporation.

I. T. Horváth. (2015). *Development and applications of the Light Extinction Spectroscopy technique for characterizing small particles* (Unpublished doctoral dissertation). Universite Libre de Bruxelles.

Kähler, C., & Scholz, U. (2006). Transonic jet analysis using long-distance micro piv. In *12th international symposium on flow visualization.*

Karthick, S., Gopalan, J., & Reddy, K. (2016). Visualization of supersonic free and confined jet using planar laser mie scattering technique. *Journal of the Indian Institute of Science*, *96*(1), 29–46.

Keane, R. D., & Adrian, R. J. (1989). Optimization of particle image velocimeters. In *International congress on applications of lasers & electro-optics* (pp. 141–161).

Meyer, K. E., Cavar, D., & Pedersen, J. M. (2007). Pod as tool for comparison of piv and les data. In *7th international symposium on particle image velocimetry* (Vol. 7, pp. 1–12).

Nobach, H., & Honkanen, M. (2005). Two-dimensional gaussian regression for sub-pixel displacement estimation in particle image velocimetry or particle position estimation in particle tracking velocimetry. *Experiments in Fluids*, *38*(4).

OSHA. (1999-2023). *Instruction TED 01-00-015* (Tech. Rep. No. Section IV: Chapter 3). Occupational Safety and Health Administration.

Pope, S. B. (2001). Turbulent flows. *Measurement Science and Technology*, *12*(11), 2020–2021.

Prasad, A., Adrian, R., Landreth, C., & Offutt, P. (1992). Effect of resolution on the speed and accuracy of particle image velocimetry interrogation. *Experiments in Fluids*, *13*, 105–116.

Price, T. J. (2022). *Experimental investigation of supersonic jets using optical diagnostics* (Unpublished doctoral dissertation). University of Tennessee.

Raffel, M., Willert, C. E., Scarano, F., Kähler, C. J., Wereley, S. T., & Kompenhans, J. (2018). *Particle image velocimetry: a practical guide*. springer.

Ragni, D., Schrijer, F., Van Oudheusden, B., & Scarano, F. (2011). Particle tracer response across shocks measured by piv. *Experiments in fluids*, *50*, 53–64.

Regert, T., Horvath, I., Buchlin, J.-M., Masutti, D., Olivier, C., Vetrano, M. R., … Le Gallic, C. (2017). Study on breakup of liquid ligaments in hypersonic cross flow using laser sheet imaging and infrared light extinction spectroscopy. In *European conference for aeronautics and space sciences (eucass), location: Krakow (poland)* (pp. 229–250).

Santiago, J. G., Wereley, S. T., Meinhart, C. D., Beebe, D., & Adrian, R. J. (1998). A particle image velocimetry system for microfluidics. *Experiments in fluids*, *25*(4), 316–319.

Scarano, F. (2001). Iterative image deformation methods in piv. *Measurement science and technology*, *13*(1), R1.

Scarano, F. (2003). Theory of non-isotropic spatial resolution in piv. *Experiments in Fluids*, *35*, 268–277.

Scarano, F. (2007). Overview of piv in supersonic flows. *Particle Image Velocimetry: New Developments and Recent Applications*, 445–463.

Scarano, F., & Riethmuller, M. L. (1999). Iterative multigrid approach in piv image processing with discrete window offset. *Experiments in Fluids*, *26*, 513–523.

Sharmishtha, C., & Utpal, B. (2017). Review of jets in a cross flow-experimental and numerical approach. *Int. J. Eng. Adv. Technol.*, *7*(2), 114–128.

Stamhuis, E., & Thielicke, W. (2014). Pivlab–towards user-friendly, affordable and accurate digital particle image velocimetry in matlab. *Journal of open research software*, *2*(1), 30.

Westerweel, J., Dabiri, D., & Gharib, M. (1997). The effect of a discrete window offset on the accuracy of cross-correlation analysis of digital piv recordings. *Experiments in fluids*, *23*(1), 20–28.

Westerweel, J., Geelhoed, P., & Lindken, R. (2004). Single-pixel resolution ensemble correlation for micro-piv applications. *Experiments in fluids*, *37*(3), 375–384.

Willert, C. (2008). Adaptive piv processing based on ensemble correlation.

Zhang, X., & Wang, J. (2022). Atmospheric dispersion of chemical, biological, and radiological hazardous pollutants: Informing risk assessment for public safety. *Journal of Safety Science and Resilience*, *3*(4), 372–397.